THREE DIMENSIONAL OPTICAL PROFILOMETRY USING A FOUR-CORE OPTICAL FIBER

by
KARAHAN BULUT

Submitted to the Graduate School of Engineering and Natural Sciences
in partial fulfillment of
the requirements for the degree of
Master of Science

Sabanci University
June 2004

THREE DIMENSIONAL OPTICAL PROFILOMETRY
USING A FOUR-CORE OPTICAL FIBER

APPROVED BY:

Assoc. Prof. Dr. M.Naci İnci ……
(Dissertation Supervisor)

Prof. Dr. Gülen Aktaş ……

Asst. Prof. Dr. İ.İnönü Kaya ……

DATE OF APPROVAL: ……

ACKNOWLEDGEMENTS

My thesis advisor Dr. Naci Inci's unlimited tolerance and respectful interest has always been a strong intensive while doing this project.

I would like to thank Dr. Canan Baysal who has always believed in my success at Sabanci University.

Mehmet Bozkurt's discipline and eruditeness has always enlightened my academic career.

Lastly, of course, my family and Güneş Avcı were always in my heart and will be.

ABSTRACT

This study describes the use of a four-core optical fiber for the first time for measurements of three-dimensional rigid-body shapes. A fringe pattern, which was generated by the interference of four wavefronts emitted from the four-core optical fiber, was projected on an object's surface. The deformed fringe pattern containing the information of the object's height was captured by a digital CCD camera. The two-dimensional Fourier transformation was applied to the image, which was digitized by using a frame grabber. After filtering this data in its spatial frequency domain by applying a bandpass filter, the two-dimensional inverse Fourier transformation was applied. A phase-unwrapping algorithm was applied to convert this discontinuous phase data to a continuous one. Finally, the shape information of the object was determined. The two-dimensional Fourier transformation analysis used in this study permitted a better signal separation and a better noise reduction. Compared to other optical profilometry techniques, which are based on fiber optics, the use of a four-core optical fiber in this study ruled out the necessity for using a fiber coupler and the alignment of fiber ends. Thus, it increased the compactness and the stability of the fringe projection system.

ÖZET

Bu çalışma, literatürde ilk kez dört-çekirdekli bir fiber optik kablo kullanarak üç boyutlu katı cisimlerin şekilllerinin nasıl ölçüleceğini tarif etmektedir. Fiber optik kablodan çıkan ve küre biçiminde olan dört adet özdeş ışık dalgasının girişimi sonucu, düzenli bir yapıda ışık saçakları(deseni) oluşturulmuş ve bu düzgün desen, katı bir cisimin üzerine tutulmuştur. Bu düzenli ışık deseni, cisimin yüksekliğinden dolayı bozulmuş, ve cismin şeklini içeren bu bilgi bir dijital kamera kullanılarak görüntülenmiştir. Görüntülenen bu resim bir görüntü yakalama kartı ile dijital bilgi haline getirilmiş ve ardından bu bilginin iki boyutlu Fourier dönüşümü alınmıştır. Uzaysal frekans bölgesinde, sadece belli frekans bandlarını geçiren bir filtre kullanarak, cisimin yüksekliğini barındıran frekans bandı izole edilerek, ve bu bilginin iki boyutlu ters Fourier dönüşümü alınmıştır. Elde edilen faz bilgisinin düzenli aralıklarla yaptığı faz atlamaları bir faz çözme algoritması kullanarak düzenli hale getirilmiştir. Böylece, cisimin üç boyutlu şekli bu düzenli faz bilgisi ışığında açığa çıkmıştır. Bu çalışmada kullanılan iki boyutlu Fourier dönüşümü, sinyalin daha iyi ayrılmasına ve parazitinin azalmasına yol açmıştır. Diğer fiber optik tabanlı yüzey kesit ölçüm teknikleri ile karşılaştırıldığında, bu çalışmada kullanılan dört çekirdekli fiber optik kablo, optik sinyali eşit olarak bölen fiber optik kuplör devre elemanının kullanılması ve fiber uçlarının hizalanması zorunluluğunu ortadan kaldırmış, ve böylece kullanılan yüzey ölçüm sistemi daha ufak ve daha kararlı hale gelmiştir.

TABLE OF CONTENTS

LIST OF FIGURES

THREE DIMENSIONAL OPTICAL PROFILOMETRY USING A FOUR-CORE OPTICAL FIBER

by
KARAHAN BULUT

Submitted to the Graduate School of Engineering and Natural Sciences
in partial fulfillment of
the requirements for the degree of
Master of Science

Sabanci University
June 2004

THREE DIMENSIONAL OPTICAL PROFILOMETRY
USING A FOUR-CORE OPTICAL FIBER

APPROVED BY:

Assoc. Prof. Dr. M.Naci İnci ……
(Dissertation Supervisor)

Prof. Dr. Gülen Aktaş ……

Asst. Prof. Dr. İ.İnönü Kaya ……

DATE OF APPROVAL: ……

ACKNOWLEDGEMENTS

My thesis advisor Dr. Naci Inci's unlimited tolerance and respectful interest has always been a strong intensive while doing this project.

I would like to thank Dr. Canan Baysal who has always believed in my success at Sabanci University.

Mehmet Bozkurt's discipline and eruditeness has always enlightened my academic career.

Lastly, of course, my family and Güneş Avcı were always in my heart and will be.

ABSTRACT

This study describes the use of a four-core optical fiber for the first time for measurements of three-dimensional rigid-body shapes. A fringe pattern, which was generated by the interference of four wavefronts emitted from the four-core optical fiber, was projected on an object's surface. The deformed fringe pattern containing the information of the object's height was captured by a digital CCD camera. The two-dimensional Fourier transformation was applied to the image, which was digitized by using a frame grabber. After filtering this data in its spatial frequency domain by applying a bandpass filter, the two-dimensional inverse Fourier transformation was applied. A phase-unwrapping algorithm was applied to convert this discontinuous phase data to a continuous one. Finally, the shape information of the object was determined. The two-dimensional Fourier transformation analysis used in this study permitted a better signal separation and a better noise reduction. Compared to other optical profilometry techniques, which are based on fiber optics, the use of a four-core optical fiber in this study ruled out the necessity for using a fiber coupler and the alignment of fiber ends. Thus, it increased the compactness and the stability of the fringe projection system.

ÖZET

Bu çalışma, literatürde ilk kez dört-çekirdekli bir fiber optik kablo kullanarak üç boyutlu katı cisimlerin şekilllerinin nasıl ölçüleceğini tarif etmektedir. Fiber optik kablodan çıkan ve küre biçiminde olan dört adet özdeş ışık dalgasının girişimi sonucu, düzenli bir yapıda ışık saçakları(deseni) oluşturulmuş ve bu düzgün desen, katı bir cisimin üzerine tutulmuştur. Bu düzenli ışık deseni, cisimin yüksekliğinden dolayı bozulmuş, ve cismin şeklini içeren bu bilgi bir dijital kamera kullanılarak görüntülenmiştir. Görüntülenen bu resim bir görüntü yakalama kartı ile dijital bilgi haline getirilmiş ve ardından bu bilginin iki boyutlu Fourier dönüşümü alınmıştır. Uzaysal frekans bölgesinde, sadece belli frekans bandlarını geçiren bir filtre kullanarak, cisimin yüksekliğini barındıran frekans bandı izole edilerek, ve bu bilginin iki boyutlu ters Fourier dönüşümü alınmıştır. Elde edilen faz bilgisinin düzenli aralıklarla yaptığı faz atlamaları bir faz çözme algoritması kullanarak düzenli hale getirilmiştir. Böylece, cisimin üç boyutlu şekli bu düzenli faz bilgisi ışığında açığa çıkmıştır. Bu çalışmada kullanılan iki boyutlu Fourier dönüşümü, sinyalin daha iyi ayrılmasına ve parazitinin azalmasına yol açmıştır. Diğer fiber optik tabanlı yüzey kesit ölçüm teknikleri ile karşılaştırıldığında, bu çalışmada kullanılan dört çekirdekli fiber optik kablo, optik sinyali eşit olarak bölen fiber optik kuplör devre elemanının kullanılması ve fiber uçlarının hizalanması zorunluluğunu ortadan kaldırmış, ve böylece kullanılan yüzey ölçüm sistemi daha ufak ve daha kararlı hale gelmiştir.

TABLE OF CONTENTS

LIST OF FIGURES

1 INTRODUCTION

Measurement has always played a vital role in history, since it has been the basis for successful trade and commerce. It drives the continuous development of science, technology and industrial production. The invention of the laser in 1958 [1] signaled a leap ahead in measurement science, promoting the development of novel techniques that exploit the wave nature of light. Optical profilometry, which is one of these techniques, is a non-invasive and a highly accurate 3-D object shape mapping one. Such a technique has many applications, say, in industrial automation, quality control and robot vision, etc. There are many 3-D optical sensing methods that use structured light pattern, which include the Moiré topography [2, 3], phase measurement profilometry [4], spatial phase detection [5], and the Fourier Transform Profilometry (FTP) [6, 7].

In this work, FTP technique is employed to process the structured light pattern. The light pattern is generated using a four-core optical fiber for the shape measurements of various rigid-bodies. As it is known that in the FTP method, a grating pattern is projected onto an object surface, and the deformed fringe pattern, which contains information of the object's surface topography, is Fourier transformed. After filtering the Fourier transformed data in its spatial frequency domain and applying the inverse Fourier transform, the shape information of the object is determined. Compared to a 1-D Fourier transform, it was shown that the FTP method can be refined by applying a 2-D Fourier transform [8] – used in this work here – which permits a better separation of the desired depth information components from those unwanted ones. In addition, only one or two deformed fringe patterns are sufficient to apply the FTP technique for a real-time data acquisition process.

The use of fiber optics is a preferable way in many 3-D optical mapping systems, since it permits the optical setup to be more compact and more stable compared to other fringe projection systems. In optical profilometry techniques, which are based on fiber optics, fringe patterns are produced by interference of two separate waveguide fiber optic point sources [9-11]. Construction of such a two-fiber optic source has requirement of using a fiber coupler. The two individual fiber ends of a 2x2 (or 1x2) fiber coupler must be carefully aligned and fixed together to control polarization for increasing the visibility of interference fringes. External disturbing factors such as vibration or thermal fluctuations may change the orientation and the distance of these fiber ends with respect to each other; thus may result in a poor fringe visibility and distortion of the fringe pattern. A poor fringe visibility limits the resolution of the system. The necessity for using a fiber coupler and the alignment of fiber ends can be ruled out by using a two-core or a multicore optical fiber, which also reduces the system's cost and its bulkiness. Gander *et al* [12] carefully demonstrated that a four-core optical fiber could be employed in a two-axis bend measurement. In addition, a two-core optical fiber was used in construction of an optical probe for flow measurement in a biomedical application [13].

In this work, for the first time, the use of a four-core optical fiber is demonstrated in an optical profilometry system for 3-D shape measurements. The fringe pattern generated by interference of four wave fronts emitted from each core of a four-core optical fiber is projected on the object surface. The deformed fringe pattern containing the object's topography is 2-D Fourier transformed. After filtering in its spatial frequency domain via a 2D Hanning window and applying the inverse Fourier transform, the surface topography of the object is easily determined. The results show that the proposed interferometric scheme is promising for 3D measurements and its sensitivity can be further developed by manufacturing suitable multicore optical fibers.

Chapter 2 of the thesis provides some further background about surface profiling by interferometry, Fourier transform profilometry and describes the phase unwrapping procedure in detail. Chapter 3, first of all, gives an overview of the Fourier Transform Method of a two-point source and then introduces the detailed fringe analysis of a four-core

optical fiber. Chapter 4 gives a detailed description of the conducted experiment and shows some sample results. This is followed by a discussion of the system performance. Finally, Chapter 5 presents the conclusions and the suggestions for future work.

2 REVIEW

The shape and the texture of the surface have a great impact on the performance of the functional applications, for example in the fields of friction, wear, lubrication, painting, bearing surfaces, biomedical, optics, integrated circuits etc. [14]. Creating perfect textures and shapes on such applications requires some precise ways of measuring the shape of these objects. Analysis of surface topography has therefore attracted much attention and has long been in use by both industry and academia. It must be here mentioned that the surface topography has gone by several names such as 3-D surface mapping [15], profilometry [16], range imaging [17], depth mapping [17], etc, and these names are interchangeably used in the literature.

The surface profiling systems can be broadly categorized into two categories, contact and non-contact measurements. 3D mapping systems based on contact measurement are also known as stylus-based systems. For many years, they have been the most widely used instruments in industry, especially in the automotive and metal-related industries. However, there is a strong tendency towards using non-contact measurement devices because of the great advantages associated with them. Unlike their contact counterparts, no physical contact is made with the specimen, which in turn avoids damage to the surface. Another advantage of non-contact measurement devices is that they have a higher vertical resolution than stylus-based ones; however it must be noted that their measurement range is smaller than stylus ones. Therefore, non-contact measurement systems are particularly preferable in areas, such as in optics, integrated electronic circuits and painting, where high precision is indispensable.

2.1 Surface Profiling by Interferometry

For many decades, optical interferometry has been used to measure the profile of an object [18] and a vast number of different kinds of interferometers have been developed [18, 19]. However, until the mid-1970s, these interferometric techniques were impractical since a large amount of human operators were required to input the great number of measurements by hand and also to assess these numbers appropriately. By the exponential growth in the power of digital computers with great image processing capabilities, optical interferometry has turned out to be one of the most popular profiling techniques used to measure 3-D surface topography. Interferometric devices are now routinely employed in some applications, such as profiling optical components and magnetic tapes [20-22].

The basic concept of interferometry is to measure phase differences between two interfering light waves. If the crest of one wave overlaps with the trough of the other, the interference is destructive and the waves cancel out. In contrast, if two crests or two troughs coincide, i.e. constructive interference, the waves strengthen each other. Then, as shown in Figure 2.1, an optical fringe pattern with parallel bright and dark bands is generated.

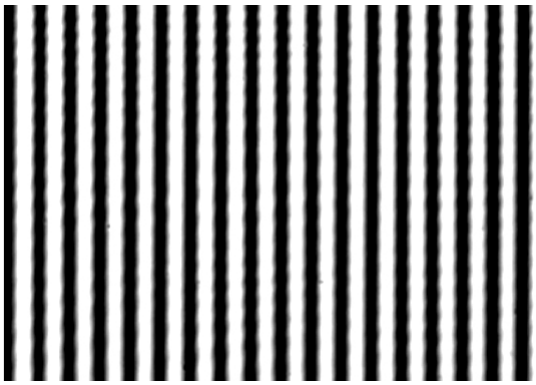

Figure 2.1. Representative fringe pattern with parallel bright and dark bands

The spatial relation between the two beams gives detailed information about the topography of the surface. In fact, if an ideally flat surface were measured with an interferometer, the fringes in the obtained interferograms would be straight-lined and equally spaced from each other. If the surface being measured had a characteristic

topography, for example, not a flat one, the fringe pattern would be deformed and each undulations of this pattern would reveal the peaks and valleys of the profile of the tested object. Therefore, the aim of interferometric instruments is to interpret the deformed fringe pattern and assess this data to produce the 3-D surface topography.

There are a large number of commercial interferometers, which are used in industry and academia. In terms of their profiling mechanisms, these devices can be classified in two main categories. The interferometers in the first category, such as Michelson, Fizeau, Mirau and Linnik, measures surface topography height directly. The second-class interferometers, for example, Nomarski interferometer, measure the slope of the surface. The former group interferometers have the benefit of getting surface height directly; however, they are very sensitive to mechanical vibration, air turbulence and temperature fluctuations. The second-class interferometers – Nomarski type- has the advantage of being sensitive to surface height variations and less influenced by environmental vibration.

In recent years, some interferometric techniques, such as, phase shifting [23, 24], Fourier transform profilometry [6, 7], heterodyne [25, 26], common-path polarization [27], differential interference contrast [28] and scanning differential interferometry [29, 30] have led to the development of new surface profiling instruments.

2.2 Fourier Transform Profilometry

Amongst non-contact 3-D surface topography methods, Fourier transform profilometry is a popular one, where a Ronchi grating or sinusoidal grating pattern is generated and projected onto a three dimensional surface. Then, the deformed fringe pattern, which contains the object's topography information, is captured by a Charge Couple Device (CCD) camera. This digital data is Fourier transformed and a suitable bandpass filter is applied in spatial frequency domain. After applying inverse Fourier transform, the discontinuous phase data is obtained. Finally, the shape information can be decoded by a phase unwrapping algorithm, which is necessary to convert this discontinuous phase to a continuous one. The phase unwrapping procedure and the detailed algorithm of

Fourier transform profilometry will be discussed further in Section 2.3 and in Section 3.1, respectively.

This elegant procedure was proposed as an alternative to Moiré contouring technique by Takeda et al. [6, 7] in 1982. The inspiration of the FTP stemmed from the observation that Moiré contouring technique was originally developed for fringe analysis by human observation rather than computer processing which in turn resulted in a great number of cumbersome requirements. Compared with the Moiré technique, FTP has a much higher sensitivity and can accomplish fully automatic distinction between a depression and an elevation on the object surface. It has no requirement for assigning fringe orders or fringe center determination, and interpolating data between contour fringes because it gives height distribution at every pixel over the entire fields. Moreover, FTP technique is free from errors induced by spurious Moiré fringes produced by the higher harmonic components of the grating pattern [6, 7].

When compared to other widespread techniques, for example, the phase-measuring profilometry (PMP) and modulation measurement profilometry (MMP), FTP requires only a single fringe pattern, which makes real-time data and dynamic data processing possible. Unlike FTP, PMP and MMP algorithms have the necessity of many fringe pattern images, which must be captured in a mechanically and optically stable environment during the time the phase is introduced. This is generally accomplished either by mechanically moving a mirror, or by some electro–optic device, which in turn increases the cost and bulkiness of the system.

Although several advantages of FTP technique have been mentioned here, the requirement of relatively long computation time and the need for manual intervention in the filtering and unwrapping operations can be considered as the main shortcomings of this method.

After Takeda et al. the FTP method has been extensively studied by many groups. Bone et al. refined this method by applying 2-D Fourier transform which permits better

separation of the desired depth information components from unwanted noises than a 1-D transform [8]. This technique has been further developed by filtering the frequency domain via a 2-D Hanning window which provided a better separation of the height information from noise when speckle-like structures and discontinuities exist in the fringe pattern [31]. FTP based on time delay and integration (TDI) camera can be used to measure 360^{o} shape [32]. To sum up, with the development of high resolution CCD cameras and personal computers with high computational performance, FTP has become an essential 3-D surface topography measurement method.

2.3 Phase Unwrapping

A generalized expression for an interferogram, i.e. the recorded intensity image, can be written as

$$I(x,y) = a(x,y) + b(x,y)\cos\phi(x,y) \tag{2.1}$$

where $a(x, y)$ is the slowly varying background intensity, $b(x, y)$ is the intensity modulation and $\phi(x, y)$ is the phase related to the physical quantity being measured. All these method give rise to an equation of the form

$$\theta = \tan^{-1}\left(\frac{C}{D}\right) \tag{2.2}$$

here C and D are functions of the recorded intensity from a set of interferograms.

Since the inverse tangent function will give phase values in the range $-\pi \le \phi \le \pi$, the solution for ϕ is a saw-tooth function, and then discontinuities occur every time ϕ changes by 2π. The term "phase unwrapping" takes place because the final step in the fringe pattern measurement procedure is to unwrap the phase along a line (or a path) counting the 2π

discontinuities and adding 2π each time the phase angle jumps from 2π to zero or subtracting 2π if the change is from zero to 2π. Figure 2.2 summarizes this process.

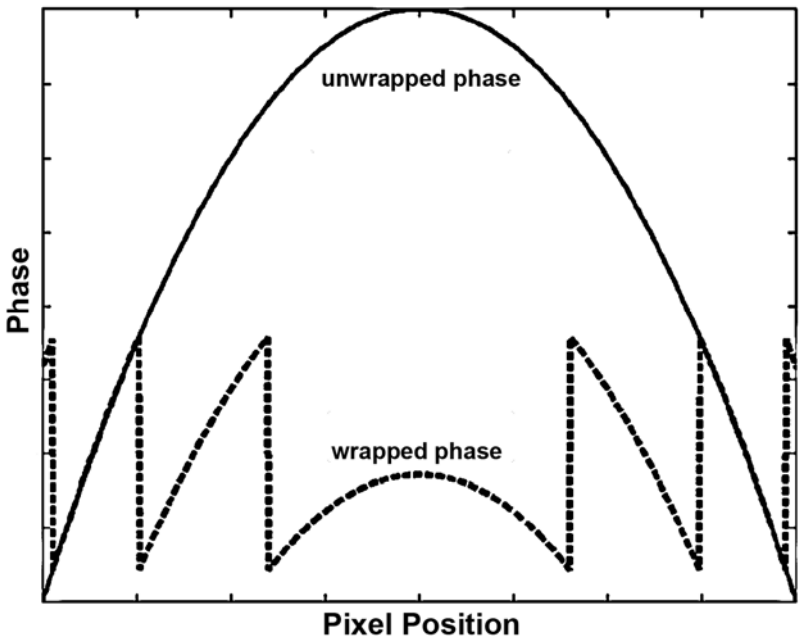

Figure 2.2. Illustration of Phase Unwrapping process

The unwrapping problem is trivial for phase maps calculated from good fringe data, so that the simple procedure explained above, i.e. detecting the phase jumps and integrating them, will be adequate for these consistent phase maps. However, we do not live in a perfect world. Low signal-to-noise ratio of the image caused by electronic noise or speckle noise, violation of the Nyquist sampling condition, and object discontinuities may lead to the false identification of phase jumps. Therefore, several sophisticated phase unwrapping algorithms have been developed for automatically detecting and compensating for these problems, some of which will be summarized in the following section. It is obvious from this discussion that phase unwrapping is a generic class of problem, fundamental to the calculation of all interferograms involving the interference of two sinusoidal waves.

2.3.1 Phase Unwrapping Techniques

The basic principle of phase unwrapping is to 'integrate' the wrapped phase data along a path, which was firstly proposed by Itoh [33]. As long as the route does not pass through a phase discontinuity, this procedure is independent of the route chosen. Thus, the success of phase unwrapping underlies in the route chosen. The logical extension of this fact is to integrate the phase along all possible paths between any two points. In this context, the phase unwrapping methods may be divided into two categories: path-dependent methods and path-independent methods.

2.3.1.1 Path-dependent methods

A sequential scan through the wrapped phase data can be considered as the simplest of all other phase unwrapping algorithms. In this approach, a 2-D data set is treated like a folded 1-D data set. However, this path-dependent approach is successful when applied to high-quality data. In the presence of noise, more sophisticated algorithms are necessary, such as, spiral scanning by Vrooman and Mass [34], multiple scan directions by Robinson and Williams [35], and counting around defects by Huntley [36].

Schorner et al. [14] proposed pixel queuing method for avoiding phase errors propagating through the data array. In this method, the regions of small phase gradients and low noise data are unwrapped first, so that data propagation errors are confined to small regions.

Another path-dependent procedure is to divide the image into segments containing no phase ambiguities (Kwon et al. [37]) or to segment the data array into square tiles or sub-arrays (Towers et al. [38]). Then the phase information at the edges of neighboring regions are compared and arranged based on the difference value that most edge pixels agree on.

2.3.1.2 Path-independent Methods

The term path independent phase unwrapping can be used to describe a method that unwraps the data by following all possible paths between any two points(to verify consistent phase loops) or a method that takes a global view of the data, unwrapping it in a way that is not dependent on the route taken through the data array.

Almost all path-independent methods unwrap the data by all possible paths between any two points to provide consistent phase loops. One popular path-independent method is based on cellular automata, proposed by Ghiglia et al. [39]. “Cellular automata are simple discrete mathematical systems that can exhibit complex behavior resulting from the collective effects of a large number of cells, each of which evolves in discrete time steps according to simple local neighborhood rules.” This definition, which is quoted from Ghiglia, is a brief summary of cellular automata concept: the phase data of each pixel is modified based on the phase values of its neighbors. After several iterations, when one comes to a point where further repetitions do not change the array further, then the phase image converges to a steady state. Although this algorithm is robust and intensive, it is, however, very immune to noise and computationally expensive. It is required to do several thousand iterations through the array to unwrap even simple phase maps.

A radically different technique, global feedback approach, to path-independent phase unwrapping algorithms has been proposed by Green and Walker [40]. Instead of analyzing individual pixels, they proposed that a global view of the image can be taken as to the presence of discontinuities in the array. The underlying assumption in this method is that unwrapped phase arrays do not have sharp discontinuities in the array. This approach is analogous to a human observer adding arbitrary phase step functions to the examined data until the result ‘seems smooth and continuous to the eye’. This approach appears to be successful when detecting one or two missed phase fringes in a substantially unwrapped data region.

3 THEORETICAL ANALYSIS

Before introducing basic mathematical model of interference pattern generated by a four-core optical fiber and its related Fourier Transform Profilometry algorithm, first of all, it would be instructive to briefly review the fringe analysis method generated by a two-point optical source. This shall allow us to form a relationship between the location of the fringes and surface profile. Then, a detailed theoretical analysis of a four-point source, which is squarely arranged, will be given.

3.1 Fourier Transform Method of a Two-point source

Figure 3.1 shows a simplified geometry to build a relationship between the object's surface topography and the phase of the fringe pattern. As seen in Fig. 3.1, laser beams from the fiber ends act as two mutually coherent point sources. They will produce a system of alternating bright and dark bands, i.e. Young's interference fringes on the screen, which can be shown in Figure 2.1. Neglecting the time dependency and avoiding a reference phase, the intensity distribution across the surface can be written as [41]

$$I(x,y) = 2I_0\left[1+\cos\left(2\pi\frac{\delta}{\lambda f}\left(x\cos\theta - z(x,y)\sin\theta\right)\right)\right] \tag{3.1}$$

here I_0 is the intensity from one fiber, δ is the separation between fiber ends, λ is the wavelength of operation, f is the distance between the fiber ends and object surface, and θ is the illumination angle. Our aim is to determine $z(x, y)$, since this parameter basically gives us the variations in the object surface as a function of x and y; in other words,

z(x, y) provides us the surface topography of the object in concern.

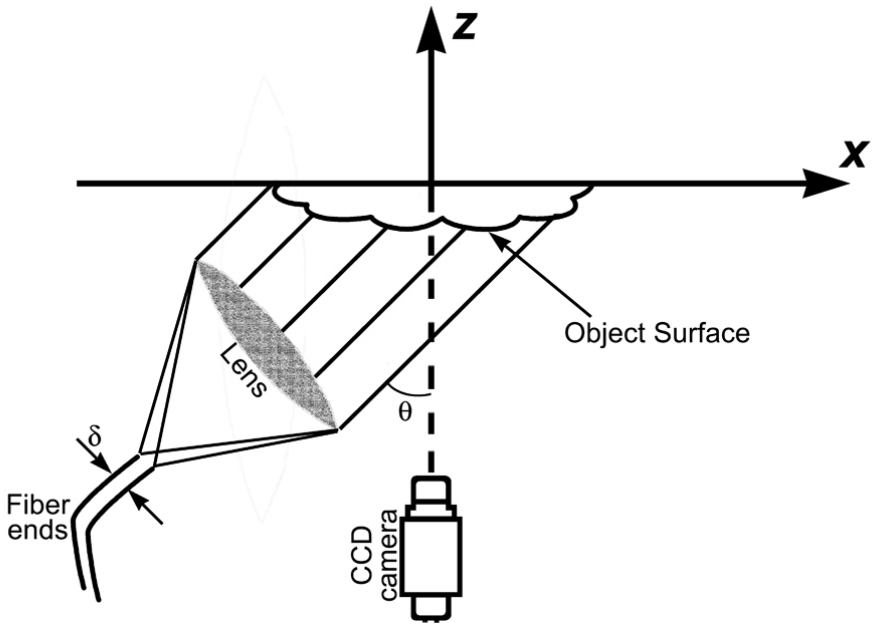

Figure 3.1. Optical geometry of a two-point source interferometric system

Equation 3.1 can be written more conveniently for the purpose of Fourier fringe analysis as,

$$I(x,y) = a(x,y) + c(x,y)\exp\left[i(2\pi u_0 x)\right] + c^*(x,y)\exp\left[-i(2\pi u_0 x)\right] \tag{3.2}$$

where

$$c(x,y) = \frac{1}{2} b(x,y)\exp\left[i\phi(x,y)\right] \tag{3.3}$$

$$u_0 = \frac{\delta}{\lambda f}\cos\theta \tag{3.4}$$

and symbol * denotes complex conjugate.

The Fourier transformation of the recorded intensity in Equation 3.2 gives

$$I(u,v) = A(u,v) + C(u-u_0,v) + C^*(u+u_0,v) \tag{3.5}$$

where *A(u,v)* and *C(u,v)* represent Fourier spectra of *a(x,y)* and *c(x,y)*, respectively. Since spatial variations of *a(x,y)*, *b(x,y)* and *φ(x,y)* change slowly, compared to spatial frequency u_0, Fourier spectra *A(u, v)*, $C(u-u_0, v)$, and $C^*(u+u_0, v)$ are separated from each other by the carrier frequency u_0 (see Figure 3.2). One of the sidelobes is isolated and translated by u_0 towards the origin as shown in Figure 3.2. *A(u, v)* and $C^*(u+u_0, v)$ are eliminated by bandpass filtering. Next, by applying the inverse Fourier transform, the complex function *c(x,y)* is obtained.

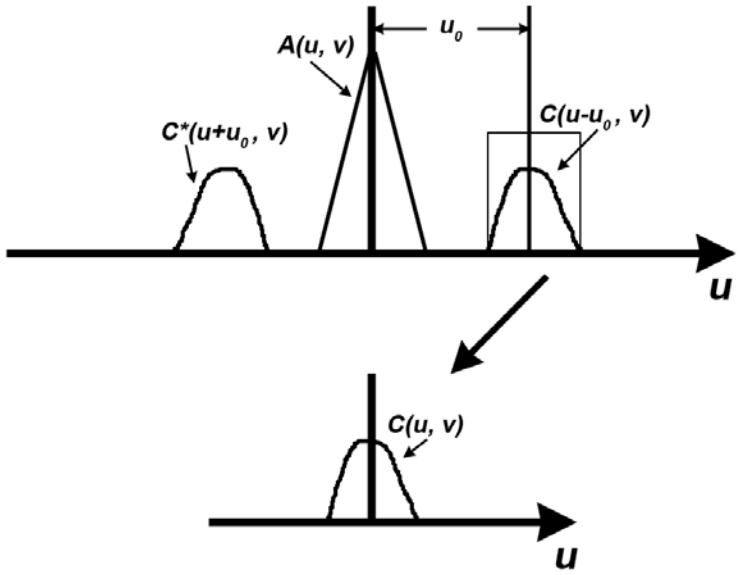

Figure 3.2. Separated Fourier spectra of a two-point source's fringe pattern

The phase may then be determined by two equivalent operations. In the first one a complex logarithm of *c(x,y)* is calculated

$$\log[c(x,y)] = \log[1/2\, b(x,y)] + i\phi(x,y) \tag{3.6}$$

Then, the phase in the imaginary part is completely separated from the amplitude variation $b(x, y)$ in the real part. In the second one, which is more commonly used, the phase is obtained by

$$\phi(x, y) = \tan^{-1}\left\{\frac{\mathrm{Im}[c(x, y)]}{\mathrm{Re}[c(x, y)]}\right\} \tag{3.7}$$

where Im[*c(x,y)*] and Re[*c(x,y)*] designate imaginary and real parts of *c(x,y)*, respectively. Since phase is wrapped into the range from $-\pi$ to $+\pi$, a phase-unwrapping algorithm is necessary to correct these 2π phase jumps. Finally, the relationship between the surface topography, that is, variations in height of the object as a function of x and y, and phase can be calculated by Equation 3.8 as

$$z(x, y) = \frac{\lambda f}{2\pi\delta \sin\theta}\phi(x, y) \tag{3.8}$$

3.2 Fringe Analysis of a Four-core Optical Fiber

3.2.1 Fourier Transform Method of a four-core optical fiber

In the section, the detailed theoretical analysis of the Fourier Transform Profilometry for a four-point source is given for the first time. This analysis consists of the mathematical formulation of interference fringe pattern, intensity distribution across the surface and phase modulation algorithm. Finally, it is shown that FTP algorithm can also be applied as well as for a four-core optical fiber.

3.2.1.1 Two-dimensional Fringe Pattern

In this study, unlike all the other conventional two source interferometric techniques which examine a stripe pattern consisting of dark and bright bands, the analyzed fringe pattern at this time is a two-dimensional spots pattern. The difference of these fringe pattern shapes can be easily seen in Figure 3.3. It is possible to obtain various types of fringe patterns by possible configurations of multiple coherent sources in space.

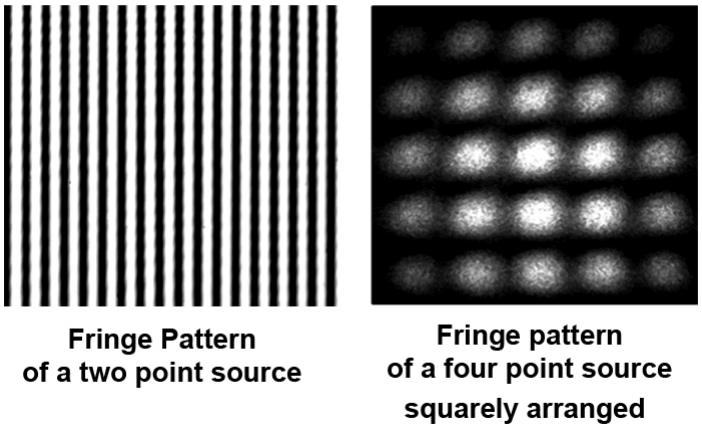

Figure 3.3. Comparison of fringe patterns

This two-dimensional spots pattern is generated by using a four-core optical fiber which was developed by HesFibel Ltd., Kayseri, Turkey [42]. A cross-sectional picture of the four-core optical fiber is shown in Figure 3.4. The fiber has four guiding cores, surrounded by a single cladding, which are squarely arranged and each core acts as an independent waveguide. In Figure 3.4, the air holes are a result of manufacturing process and are not aimed for any special purposes.

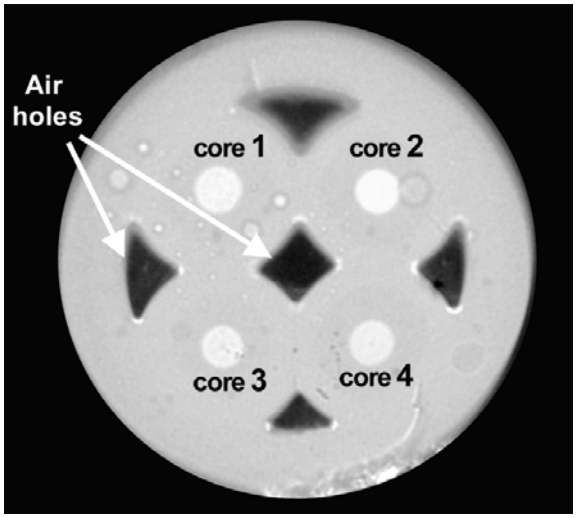

Figure 3.4. Cross-sectional picture of the cleaved face of the four-core optical fiber

Figure 3.5 shows a fringe pattern which is generated by the interference of four light beams emitted from the four-core optical fiber and its 2-D Fourier spectrum. In Figure 3.5, zero-frequency term is omitted on purpose to indicate the details of the spectrum more clearly.

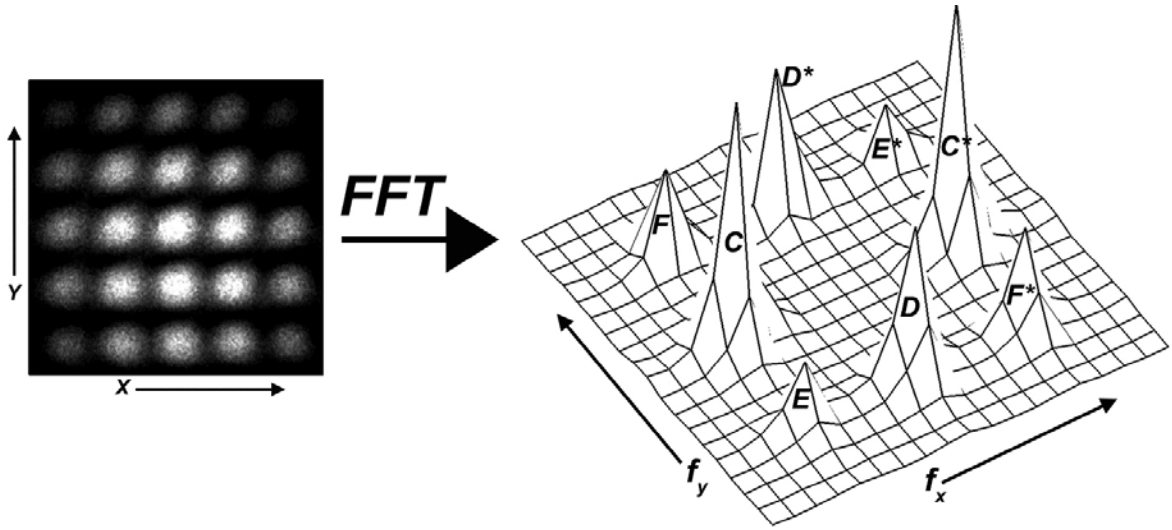

Figure 3.5. Non-deformed fringe pattern and its 2-D Fourier spectrum without zero frequency term

The six possible couplings of the four fiber cores located at the corner of a square generate four different superimposed interferograms- electronic recording of the optical interference pattern. Referring to Figure 3.6, the pairings of the cores 1-2 and 3-4 generate

one vertical interferogram, which correspond side lobe *C*; the pairings of the cores 1-3 and 2-4 generate one horizontal interferogram (side lobe *D*); and the pairings of the cores 1-4 and 2-3 generate two sets of different diagonal interferograms which correspond side lobes *E* and *F*, respectively. Superimposing of these six interferograms generate the two-dimensional fringe pattern shown in Figure 3.5. The aim of this experiment is properly extraction of the phase information from these sidelobes in the frequency domain.

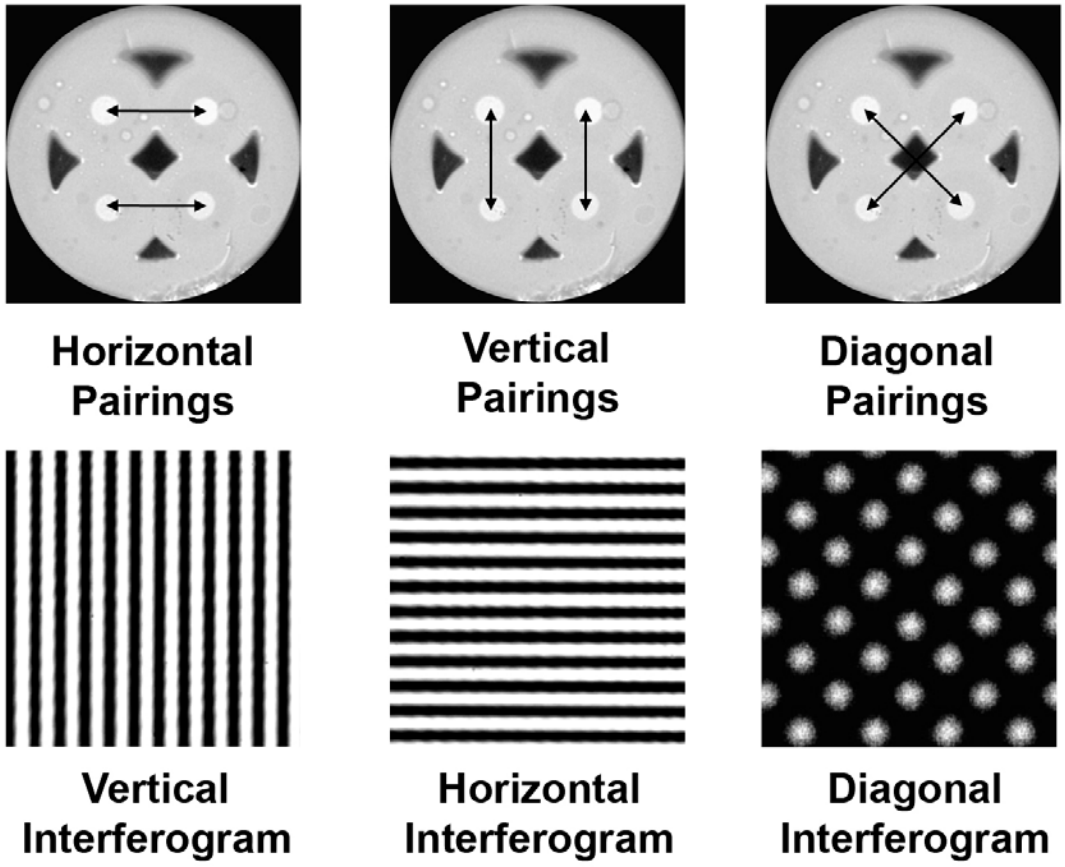

Figure 3.6. Generated interferograms of a four-core optical fiber

3.2.1.2 Intensity Distribution Analysis across the surface

The algorithm of Fourier transform profilometry requires the intensity distribution across the surface seen by camera. After Fourier transformation of this function in its spatial domain, the side lobe containing the phase information can be further processed. As seen in Figure 3.7, the four-point optical sources are located at the corners of a square. The sources are designated as *s1*, *s2*, *s3*, and *s4* in the (ρ-η) plane. Each adjacent source is separated by the distance of δ. The four monochromatic waves, which are inherently coherent, are superimposed in the (*x*-*y*) plane producing a two-dimensional interference pattern.

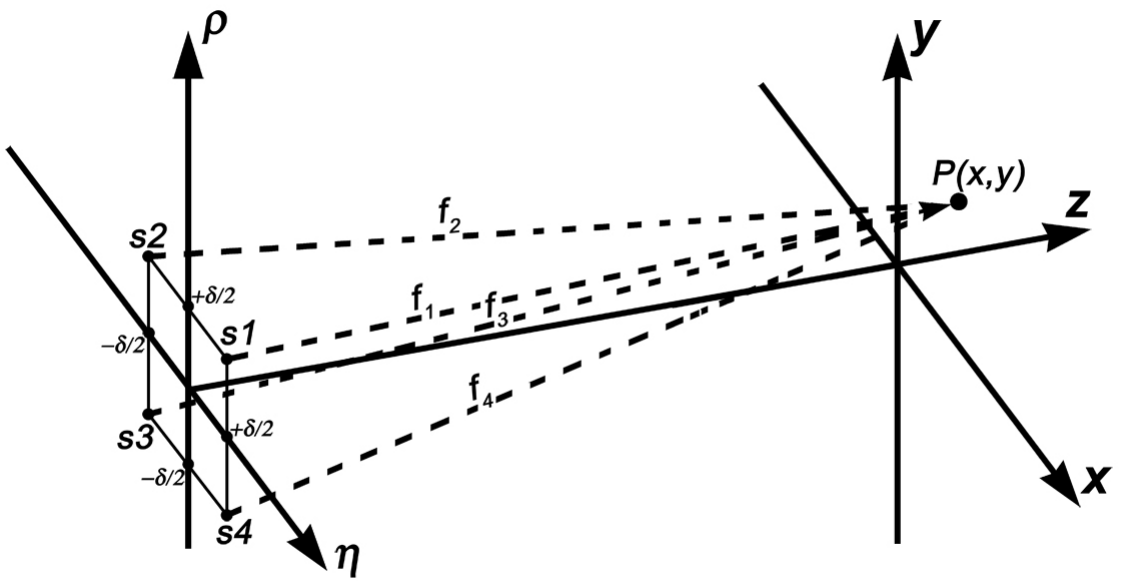

Figure 3.7. Optical geometry of the four-point source and the interference point, *P*(*x,y*)

According to the Superposition Principle, the total electric field vector of a four-point source at point *P*(*x,y*) in Figure 3.7 can be written as [43]

$$\vec{E} = \vec{E}_1 + \vec{E}_2 + \vec{E}_3 + \vec{E}_4 \tag{3.9}$$

Considering only relative irradiances within the same medium, the time average of the magnitude of the electric field vector squared gives the intensity distribution as [43]

$$I = \left\langle \vec{E}^{\,2} \right\rangle_T \tag{3.10}$$

Then, the intensity distribution across the surface for θ=0 can be written as

$$\begin{aligned} I(x,y) = 2I_0[&2 + 2\cos(k(f_2 - f_1)) + 2\cos(k(f_3 - f_1)) + \\ &2\cos(k(f_4 - f_1)) + 2\cos(k(f_3 - f_2)) + \\ &2\cos(k(f_4 - f_2)) + 2\cos(k(f_4 - f_3))] \end{aligned} \tag{3.11}$$

here I_0 is the intensity from one source, $k = \dfrac{2\pi}{\lambda}$ is the propagation constant, where λ is the wavelength, θ is the illumination angle (in this case θ is zero), and f_1, f_2, f_3, f_4 are distances from the four point sources to the object plane which are shown in Figure 3.7. In the Cartesian coordinate system, these distances can be calculated as

$$f_i = \left[(x - \eta_i)^2 + (y - \rho_i)^2 + z^2\right]^{1/2} \tag{3.12}$$

where i = 1, 2, 3, 4

Equation 3.12 can be written more conveniently as

$$f_i = f\left[1 + \frac{\eta_i^{\,2} + \rho_i^{\,2}}{f^2} - \frac{2\eta_i x + 2\rho_i y}{f^2}\right]^{1/2} \tag{3.13}$$

where

$$f = \left(x^2 + y^2 + z^2\right)^{1/2} \tag{3.14}$$

For a very large distance, $z >> (\eta, \rho, x, y)_{max}$, Equation 3.13 can be approximated to binomial expansion as

$$f_i = f + \frac{\eta_i^{\,2} + \rho_i^{\,2}}{2f} - \frac{\eta_i x + \rho_i y}{f} \tag{3.15}$$

After calculation of each distance difference, Equation 3.11 can be written as

$$\begin{aligned} I(x,y) = 2I_0\Bigg[2 + 2\cos\left(k\left(\frac{\delta x}{f}\right)\right) + 2\cos\left(k\left(\frac{\delta y}{f}\right)\right) + \\ \cos\left(k\left(\frac{\delta(x+y)}{f}\right)\right) + \cos\left(k\left(\frac{\delta(x-y)}{f}\right)\right)\Bigg] \end{aligned} \tag{3.16}$$

If we appropriately substitute Equation 3.8 into Equation 3.16 by considering the optical geometry in Figure 3.1, we obtain Equation 3.17, which is the intensity distribution across the surface seen by camera of a four-point optical source arranged in a square.

$$\begin{aligned} I(x,y) = 2I_0\Bigg[2 + 2\cos\left(2\pi\frac{\delta}{\lambda f}\left(x\cos\theta - z(x,y)\sin\theta\right)\right) + 2\cos\left(2\pi\frac{\delta}{\lambda f}y\right) + \\ \cos\left(2\pi\frac{\delta}{\lambda f}\left(x\cos\theta - z(x,y)\sin\theta + y\right)\right) + \cos\left(2\pi\frac{\delta}{\lambda f}\left(x\cos\theta - z(x,y)\sin\theta - y\right)\right)\Bigg] \end{aligned} \tag{3.17}$$

3.2.1.3 Phase Extraction

For the purpose of Fourier fringe analysis, the intensity distribution function seen by camera, given in Equation 3.17, can be written more conveniently as

$$
\begin{aligned}
I(x,y) = a(x,y) + c(x,y)\exp[i(2\pi u_0 x)] + c^*(x,y)\exp[-i(2\pi u_0 x)] + \\
d(x,y)\exp[i(2\pi u_0' y)] + d^*(x,y)\exp[-i(2\pi u_0' y)] + \\
e(x,y)\exp[i(2\pi(u_0 x + u_0' y)] + e^*(x,y)\exp[-i(2\pi(u_0 x + u_0' y)] + \\
f(x,y)\exp[i(2\pi(u_0 x - u_0' y)] + f^*(x,y)\exp[-i(2\pi(u_0 x - u_0' y)]
\end{aligned}
\tag{3.18}
$$

where $u_0^{'}$ is the carrier frequency without θ component and the two-dimensional Fourier transform of $I(x, y)$, denoted $\Im\{I(x, y)\}$, is defined by the equation [44]

$$
\Im\{I(x,y)\} = I(u,v) = \int_{-\infty}^{\infty}\int I(x,y)\exp[-i2\pi(ux+vy)]dx\,dy \tag{3.19}
$$

After two-dimensional Fourier transformation of each component in Equation 3.18 by applying the general formula given in Equation 3.19, the Fourier transformation of the recorded intensity distribution is given by

$$
\begin{aligned}
I(u,v) = A(u,v) + C(u-u_0,v) + C^*(u+u_0,v) + \\
D(u,v-u_0') + D^*(u,v+u_0') + \\
E(u-u_0,v-u_0') + E^*(u+u_0,v+u_0') + \\
F(u-u_0,v+u_0') + F^*(u+u_0,v-u_0')
\end{aligned}
\tag{3.20}
$$

where A, C, C^*, D, D^*, E, E^*, F, and F^* represent the Fourier spectrum of a, c, d, e, and f, respectively.

In this work, the fringe pattern was projected onto the object surface in such a way that only the vertical interferogram contained the object's height information as a function of x and y (i.e., $z(x,y)$). Then, if we study only the vertical interferogram and its related Fourier spectra component (that is, $C(u-u_0, v)$ term in Eq. (10)), the Fourier fringe analysis of a four-point source reduces to that of the two-point sources' case, which is described above. By applying an appropriate window, $C(u-u_0, v)$ term containing data on the object's surface topography is isolated and translated by u_0 towards the origin. Other spectral

components are eliminated by bandpass filtering. After inverse Fourier transformation, the phase data is obtained. A phase-unwrapping procedure is necessary to convert this discontinuous phase to a continuous one. Finally, the phase information of the object is extracted using Equation 3.8.

3.2.2 Spherical Distortion Analysis of the Fringe Pattern

Two-dimensional interference pattern of a four-core optical fiber has an inherent spherical distortion, which results in the misalignments of fringes. Although this error is almost not observable in the central portion of the pattern, it attains its maximum value at the outer edges. Hence, before using a multiple source, especially for a high precision application, one must carefully examine the intrinsic spherical distortions of the fringe pattern at the design stage.

The intensity distribution across the surface including the spherical distortion can be written by Equation 3.16 here. It should be noted that the camera has no effect in this analysis. Thus, the viewing angle (θ) and the phase term (ϕ) in Equation 3.16 is omitted.

$$I(x,y) = 2I_0\left[2 + 2\cos k\frac{\delta x}{f} + 2\cos k\frac{\delta y}{f} + 2\cos k\frac{\delta(x+y)}{f} + 2\cos k\frac{\delta(x-y)}{f}\right] \qquad (3.21)$$

Equation 3.21 can be written more conveniently as

$$I(x,y) = 16I_0\cos^2\left(\frac{k\delta}{2f}x\right)\cos^2\left(\frac{k\delta}{2f}y\right) \qquad (3.22)$$

Thus, from Equation 3.22, we obtain

$$x_{pr} = p\frac{\lambda f_{pr}}{\delta}$$
$$y_{pr} = r\frac{\lambda f_{pr}}{\delta} \qquad |p|,|r| = 0,1,2 \qquad (3.23)$$

This gives the position of the p[th] and r[th] bright fringes on the screen.
where

$$f_{pr} = \left(x_{pr}^2 + y_{pr}^2 + z^2\right)^{\frac{1}{2}} \qquad (3.24)$$

Here, it can be easily seen that the reason behind the shift of the fringe pattern from the desired square pattern to the spherical one is that x_{pr} and y_{pr} terms are the inputs of f_{pr}. In case of a two-source case, only x_{pr} term would be a variable of f_{pr}, which in turn would result in a less distortion shift - from a stripe pattern to an ellipsoidal one.

After solving Equations 3.23 and 3.24, the locations of the bright fringes are obtained by

$$x_{pr} = p\frac{\lambda z}{\delta}\left[1 - \frac{\left(p^2 + r^2\right)\lambda^2}{\delta^2}\right]^{-\frac{1}{2}}$$
$$y_{pr} = r\frac{\lambda z}{\delta}\left[1 - \frac{\left(p^2 + r^2\right)\lambda^2}{\delta^2}\right]^{-\frac{1}{2}} \qquad |p|,|r| = 0,1,2 \qquad (3.25)$$

From the above equation, it is seen that the fringe pattern will be squared, only when the following condition is satisfied

$$\frac{\delta}{\lambda} >> \sqrt{p_{\max}^2 + r_{\max}^2} \qquad (3.26)$$

Since, the relationship between the separation distance of the sources (δ) and the operating wavelength (λ) must be satisfied in the above equation, then, it is safe to say that the spherical distortion is an inherent problem. Moreover, the above result is not dependent on the distance of operation. If the desired square locations of the spots are taken as

$$\begin{aligned} x_{p0} &= p\frac{\lambda z}{\delta} = p\Delta x \\ y_{0r} &= r\frac{\lambda z}{\delta} = r\Delta y \end{aligned} \qquad |p|,|r| = 0,1,2 \qquad (3.27)$$

finally, by comparing Equation 3.25 with Equation 3.27, the spot position errors can be found as

$$\begin{aligned} \Delta x_{pr} &= x_{pr} - x_{p0} \cong \frac{1}{2}\left(\frac{\lambda}{\delta}\right)^2 p\left(p^2 + r^2\right)\Delta x \\ \Delta y_{pr} &= y_{pr} - y_{0r} \cong \frac{1}{2}\left(\frac{\lambda}{\delta}\right)^2 r\left(p^2 + r^2\right)\Delta y \end{aligned} \qquad |p|,|r| = 0,1,2 \qquad (3.28)$$

For a 5x5 experimentally analyzable fringe pattern, operating wavelength λ of 632.8 nm, and an effective adjacent core separation of 30 μm, then the maximum spherical distortion error can be calculated as 0.01 mm, which can be considered as not a notable effect on the performance of this system.

3.2.3 Number of Fringes

In optical profilometry systems, fringe number in an interference pattern has an important effect in terms of inspectable area and sensitivity of the system. Here, the calculation of the fringe number for a four-point source arranged in a square will be demonstrated.

The numerical aperture (NA) is a characteristic parameter of an optical fiber, which is defined by [43]

$$NA = \left(n_1^2 - n_2^2\right)^{1/2} \tag{3.29}$$

where n_1 and n_2 are the refractive indices of the core and cladding of the optical fiber, respectively.

Not all source radiation can be guided along an optical fiber. Only rays falling within a certain cone at the input of the fiber can normally be propagated through the fiber. This issue is the same for the output of an optical fiber. Therefore, the output light from an optical fiber has a fixed angle of illumination (κ) which depends on the numerical aperture of the fiber and the refractive index of the launching medium (i.e., the refractive index of the air, which is one). This is illustrated in the following equation by

$$\kappa = \arcsin\left(NA\right) \tag{3.30}$$

In this study, the two-dimensional fringe pattern is a result of the overlapping of four wavefronts emitted from the four-core optical fiber.

The illumination area of each core in the object plane (i.e., (x, y) plane) can be given by

$$\begin{aligned} A_1 &= \left\{(x,y)\left|(x-\frac{\delta}{2})^2 + (y-\frac{\delta}{2})^2 \le \left(z\tan\kappa\right)^2\right.\right\} \\ A_2 &= \left\{(x,y)\left|(x+\frac{\delta}{2})^2 + (y-\frac{\delta}{2})^2 \le \left(z\tan\kappa\right)^2\right.\right\} \\ A_3 &= \left\{(x,y)\left|(x+\frac{\delta}{2})^2 + (y+\frac{\delta}{2})^2 \le \left(z\tan\kappa\right)^2\right.\right\} \end{aligned} \tag{3.31}$$

$$A_4 = \left\{ (x,y) \middle| (x - \frac{\delta}{2})^2 + (y + \frac{\delta}{2})^2 \le (z \tan \kappa)^2 \right\}$$

The acceptance angle κ is quite small for typical single mode optical fibers, for example, in our case $\kappa = 0.14$ radians. Therefore, the following approximation can be used in this analysis

$$\tan k \approx k \tag{3.32}$$

Then, the overlapping area A (that is, $A_1 \cap A_2 \cap A_3 \cap A_4$) can be calculated as

$$\begin{aligned} A &= \left\{ (x,y) \middle| \; x^2 + y^2 \le z^2 \tan^2 \kappa - \frac{1}{2}\delta^2 \right\} \\ A &\approx \left\{ (x,y) \middle| \; x^2 + y^2 \le z^2 \kappa^2 - \frac{1}{2}\delta^2 \right\} \end{aligned} \tag{3.33}$$

Since $z >> \delta$, the above formulation can be further simplified as

$$A \approx \left\{ (x,y) \middle| \; x^2 + y^2 \le z^2 \kappa^2 \right\} \tag{3.34}$$

then the following relation is found

$$\sqrt{\left| x_{p0} \right|_{\max}^2 + \left| y_{0r} \right|_{\max}^2} \le z\kappa \tag{3.35}$$

here $max(x_{p0})$ and $max(y_{0r})$ are the spot locations at the edge of the interference pattern, which has $N \times N$ number of fringes. These spot positions can be calculated from Equation 3.27 by setting

$$p_{\max} = n_{\max} = \frac{N}{2} \tag{3.36}$$

Then, the following relation is obtained

$$\begin{aligned} \left| x_{p0} \right|_{\max} &= \left| p_{\max} \, \Delta x \right| = \frac{N}{2} \Delta x \\ \left| y_{0r} \right|_{\max} &= \left| r_{\max} \, \Delta y \right| = \frac{N}{2} \Delta y \end{aligned} \tag{3.37}$$

After substituting Equation 3.27 and Equation 3.37 into Equation 3.35, finally the desired number of fringe relation is obtained

$$N \le \frac{\delta \kappa \sqrt{2}}{\lambda} \tag{3.38}$$

For an effective adjacent core separation δ of 30 μm, acceptance angle κ of 0.14 radians, and an operating wavelength of λ =632.8 nm, the number of fringe can be approximately calculated as nine.

4 EXPERIMENT

4.1 Equipment

4.1.1 Laser

The light source was a 17mW CW (continuous wave) He-Ne laser (Melles Griot 05-LHP-925, USA) which has an output of 632.8 nm red light. It produces linearly polarized light, which has a coherence length of 30 cm. The laser beam has a divergence of 0.83 mrad. This type of He-Ne laser was preferred for this study, since its output beam has a high power, a low divergence angle, and a high coherence length, which are the most important factors affecting the performance of an optical profilometry system.

4.1.2 Camera

The deformed fringe patterns were captured by a Charge Couple Device (CCD) camera (Redlake Inc. Kodak Megaplus 1.6i, USA). It is a high-resolution (1534 x 1024-pixel array with 9 x 9-μm square pixels) CCD camera with a 10-bit digital output and an internal thermal electric cooling. The camera's high resolution and controllable exposure time capabilities provided high quality digital images. Therefore, in this work, the 3-D mapping data values of an object were less affected by noise, which in turn resulted in highly reliable results.

4.1.3 Frame Grabber

The video signal from CCD camera was received and digitized by using a frame grabber (Epix Inc. PIXCI D2X, USA) which is a 32-bit PCI bus master board.

4.1.4 Optical Fiber

The single mode four-core optical fiber was manufactured in HesFibel Ltd., Kayseri, TURKEY. Each fiber core has a diameter of 10.6 μm and the adjacent center-center core separation is 40.6 μm. The cut-off wavelength of each core is about 1250 nm. The cores are surrounded with a 125 μm single cladding.

4.1.5 Optical Components

4.1.5.1 Mirror

The laser beam was directed by a broadband aluminum coated mirror (Thorlabs Inc. PF-10-03-F01, USA). The mirror has a 25.4 mm diameter and about 90% reflection at 632.8 nm.

4.1.5.2 Plano-Convex Lens

To provide constant fringe spacing, a plano convex collimating lens (Thorlabs Inc. LA1229, USA) was used. The lens has a diameter of 25.4 mm and a clear aperture of >90% with a focal point of f =175 mm which has a tolerance of ±1%.

4.1.5.3 CCD Lens

The deformed fringe pattern images were carried on the CCD chip with the aid of a macro-lens (Computar MLH-10X, USA) which has a focal point of 130 mm.

4.1.6 Nanopositioning Stage

The laser beam was launched into the fiber cores by a nanopositioning stage (Melles Griot 17 AMB 003/MD, USA).

4.1.7 Fiber Rotator

The fiber ends was rotated by a fiber rotator (Thorlabs Inc. MDT718-125, USA) to orient the fringe pattern in such a way that it will be congruent with the object plane.

4.1.8 Computer

The digitized images were processed by a personal computer, which has a 2.4 GHz Pentium class CPU, and a 512 MB of RAM.

4.1.9 Software

All data processing operations, such as Fourier transformation or phase unwrapping, were done by a software program (MathWorks Inc. Matlab Version 6.5.0.180913a (R13), USA).

4.2 Experimental Setup

The experimental setup used for surface profilometry measurement is shown in Fig. 4.1. Linearly polarized light from a 35 mW HeNe laser of wavelength 632.8 nm was launched into all four cores of an optical fiber simultaneously.

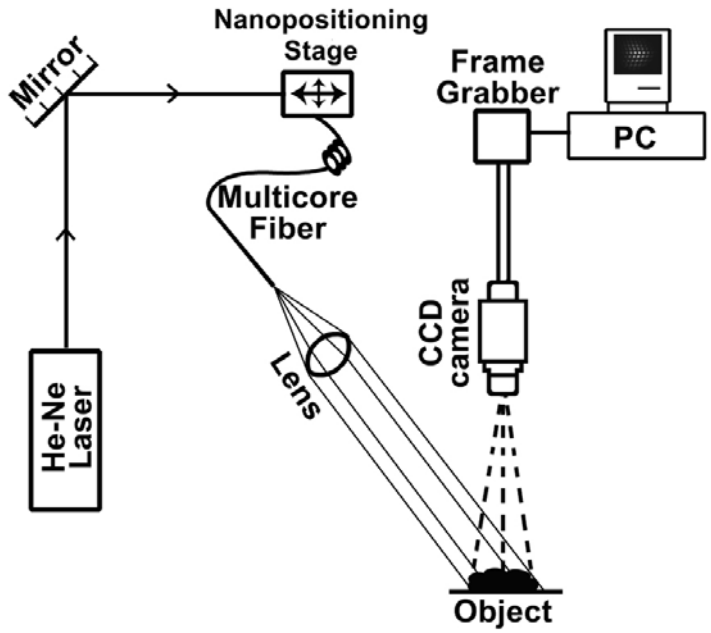

Figure 4.1. Schematic diagram of the experimental setup

A three-axis nanopositioning stage was used to launch the laser light beam into the cores for an evenly launching of optical power and also preventing the optical losses at the cores' entry. An even coupling to four cores simultaneously was essential for a good contrast of the fringe pattern; otherwise, the visibility of the fringe pattern would be poor if the optical power coupling was not uniform for all fiber cores. In addition, the four cores are carefully located at the corner of a square during the manufacturing process [42] to allow a maximum fringe contrast (i.e., to obtain the highest possible fringe visibility). Each fiber core diameter was 10.6 μm and the adjacent core separation was 40.6 μm; measured using an optical microscope. Each core, accommodated within ~125 μm common single cladding, had a cut-off wavelength of about 1250 nm, acted as an independent waveguide. The length of the four-core fiber was approximately 40 cm. The fringe pattern was formed by the interference of four wavefronts emitted from the fiber cores acting as independent point sources. The four fiber cores had a mutual coherence with each other due to a simultaneous illumination of the common HeNe laser source (see Figure 4.1). A careful cleaving of the fiber-end was performed to minimize the optical path difference between the four-waveguide sources. The four-core fiber end was placed at the focal point of a plano

convex collimating lens of focal point of f=175 mm, thus a constant fringe spacing was provided. The far-distance fringe pattern was checked carefully over 5 m to ensure that the fiber-end was precisely located at the lens' focal point. The centre of curvature of the plano-convex lens was placed in the direction of the focus and the conjugate ratio was adjusted to approximately 5:1 to minimize the spherical aberration. The deformed fringe pattern was captured by a CCD camera with a bit depth of eight for faster memory access in the computer. A macro-lens of 130 mm focal point, which had a format larger than that of the CCD's chip, was employed with the camera to enhance the optical performance of the system. Diffraction patterns caused by dust particles on lenses and mirrors were eliminated by carefully cleaning them by methanol. The CCD camera was located at a viewing angle of θ=15^{o} in order to increase the magnitude of reflected light towards the camera and to reduce the signal fades due to shadowing effects on the object surface which would result in problematic effects in the phase unwrapping algorithm. A frame grabber was used to receive and digitize the signal from the CCD camera. The digitised pixels were collected by a personal computer for further Fourier fringe processing by using Matlab software program. Then, the deformed fringe pattern images were 2-D Fourier transformed. The spectral side-lobe containing information on the object's surface topography was filtered by a 2-D Hanning window as seen in Figure 4.2.

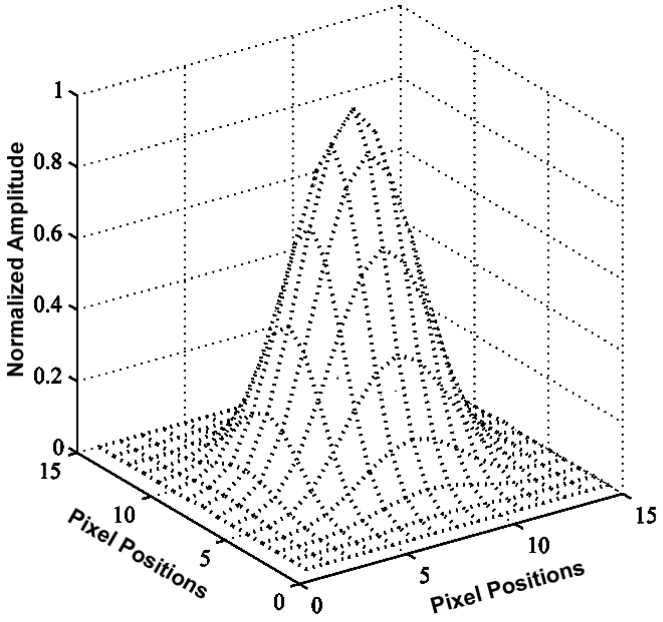

Figure 4.2. Two-dimensional Hanning window

After applying the inverse 2-D Fourier transform, the wrapped phase data was obtained. A phase-unwrapping algorithm, similar to method proposed by Itoh [33], was applied to convert this discontinuous phase to a continuous one. Finally, the surface profile of the object was determined from Equation 3.8.

4.3 Results

Various types of test objects were profiled using the four-core optical fiber interferometric system. A few of them will be demonstrated in this section. The profiled first two objects are a flat plate with a 2 mm step, and a board marker, respectively.
These two objects have well known dimensions in order to compare both real dimensions and the experimental results. The other profiled objects were a triangular shaped paper, a piece of sandstone and a sculptured head object.

4.3.1 Reconstruction of a flat plate with a 2 mm step

The first test object is a flat plate with a 2 mm step in the upper right corner. The deformed fringe pattern of the object is shown in Figure 4.3(a). A 2D Fourier transform spectra of the test object without zero frequency –that is, to demonstrate the clarity of the graph- and the reconstructed surface of the object are shown in Figure 4.3(b) and Figure 4.3(c), respectively. Side lobe D in Figure 4.3(b) was analysed by filtering it out by means of applying a 2D Hanning window and the inverse Fourier transform to reconstruct the surface topography to the object as shown in Figure 4.3(c). As seen in Figure 4.3(c), the measured profile corresponds quite well to the object's actual profile.

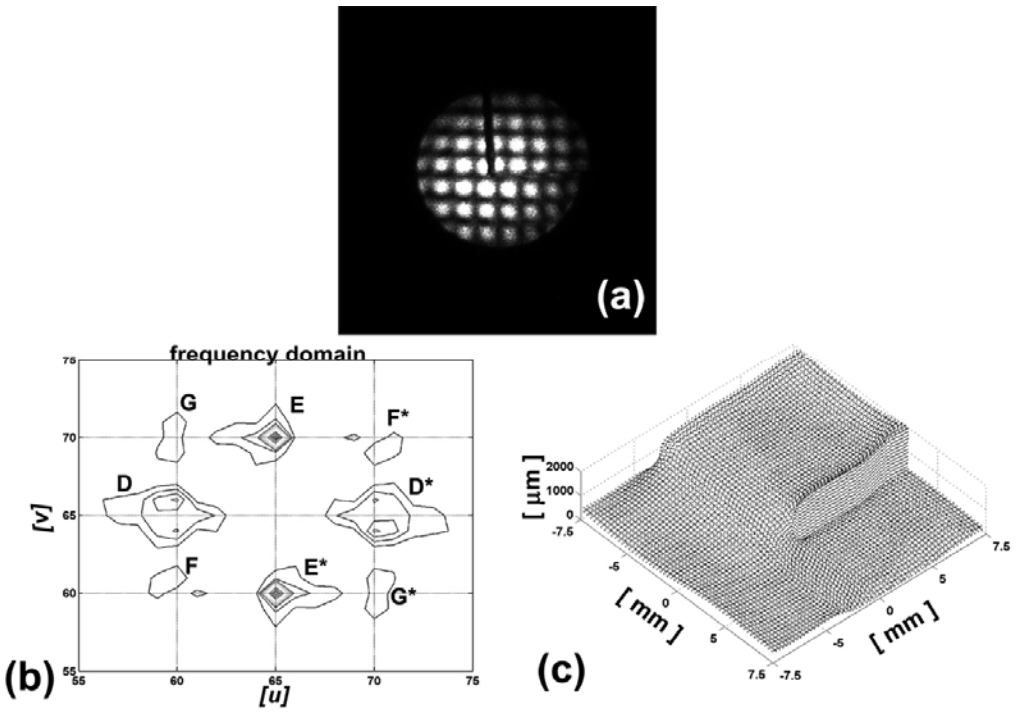

Figure 4.3. (a) Projected fringe pattern of a flat plate with a 2 mm step in the upper right corner; (b) 2D Fourier spectra of the test object without zero frequency. The analysed side lobe is *D* as shown in figure; (c) reconstructed surface of the object.

The relationship between the height of an object and its unwrapped phase data was given in Equation 3.8. Taking the derivative of this equation with respect to ϕ gives the following relation

$$\frac{dz}{d\phi} = \frac{P_0}{2\pi \sin\theta} \tag{4.2}$$

where P_0 is the fringe spacing defined by

$$P_0 = \frac{\lambda f}{\delta} \tag{4.2}$$

here λ is the operating wavelength, f is the distance between the fiber-ends and object surface, and δ is the separation between the cores.

Equation 4.1 gives the rate of change of surface height with respect to phase change. The resolution then can be determined if the detectable phase difference is known. In the ideal case, the minimum detectable phase difference should be $2\pi/256$, since all the deformed fringe pattern images presented here were taken by an 8-bit digitizer. However, because of a considerable signal to noise ratio in the system, the number of gray levels between the peak and valleys of the fringe pattern were about 100. Therefore, the minimum detectable phase difference was $2\pi/100$. Then by using Equation 5.1, the system resolution R can be calculated as [10]

$$R = \frac{P_0}{100 \sin\theta} \tag{4.3}$$

For the viewing angle θ of 15^o and the fringe spacing P_0 of 4.01 mm, the system resolution can be approximately found as 0.15 mm.

4.3.2 Reconstruction of a board marker

The second example is a board marker of 14.4 mm radius of circle; its projected fringe pattern and the reconstructed surface map are seen in Figure 4.4.

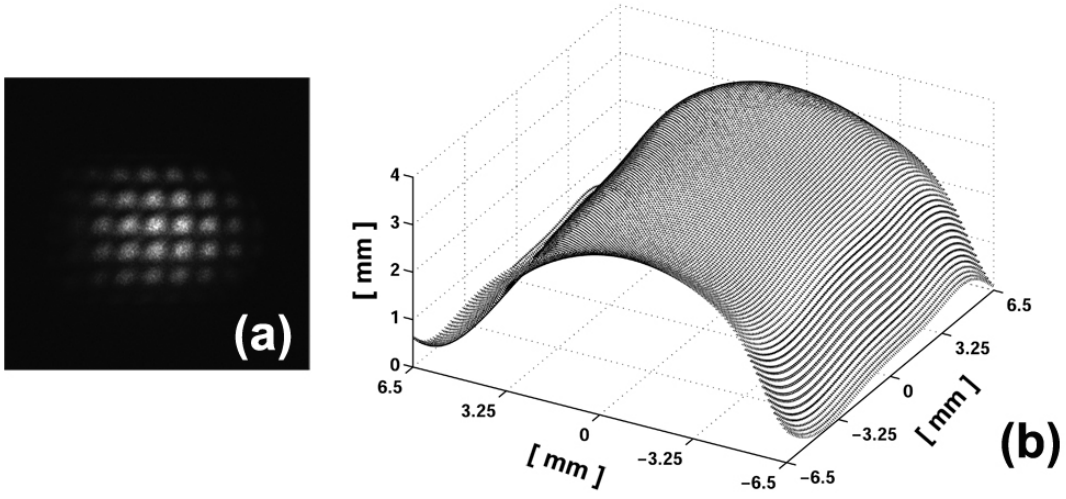

Figure 4.4. (a) Projected fringe pattern of a board marker which has a 14.4 mm circle of radius; (b) reconstructed surface of the object.

A cross section through the point of maximum surface height from the reconstructed surface can be seen in Figure 4.5.

A comparison of the results shows that the root-mean-squared (rms) error is 0.4 mm, or 11.3% of the object depth; which is in good agreement with the relationship exists between the number of fringes and rms error [45]. This error figure seems to be quite high in terms of performance of the system, when compared to similar results in previously published work [9-11]. The reason is due to the number of interference fringes being small (i.e., 7-8) and fringe spacing being more than it is desired. However, these are the preliminary results and are aimed to prove that the proposed four-core fiber scheme in optical profilometry is promising. The error margin can be easily reduced to, say, around 2% by redesigning the four-core fiber for desired number of fringes, fringe spacing and the wavelength of illumination. Another point is that the determination of the phase becomes very noise sensitive at the edges of the image due to this small number of fringes. Thus causing some kind of noticeable distortions at the edges of the reconstructed surface of the objects (see Figure 4.3(c) and Figure 4.4(b)). Therefore the number of fringes must be increased and the fringe spacing must be decreased in order to prevent these shape distortions and improve the sensitivity of the system. Choosing a larger distance of centre-to-centre fiber core separations (e.g., ~100 μm) can easily resolve such problems. A design example of multi-core fibers is given below in the discussion section of the results.

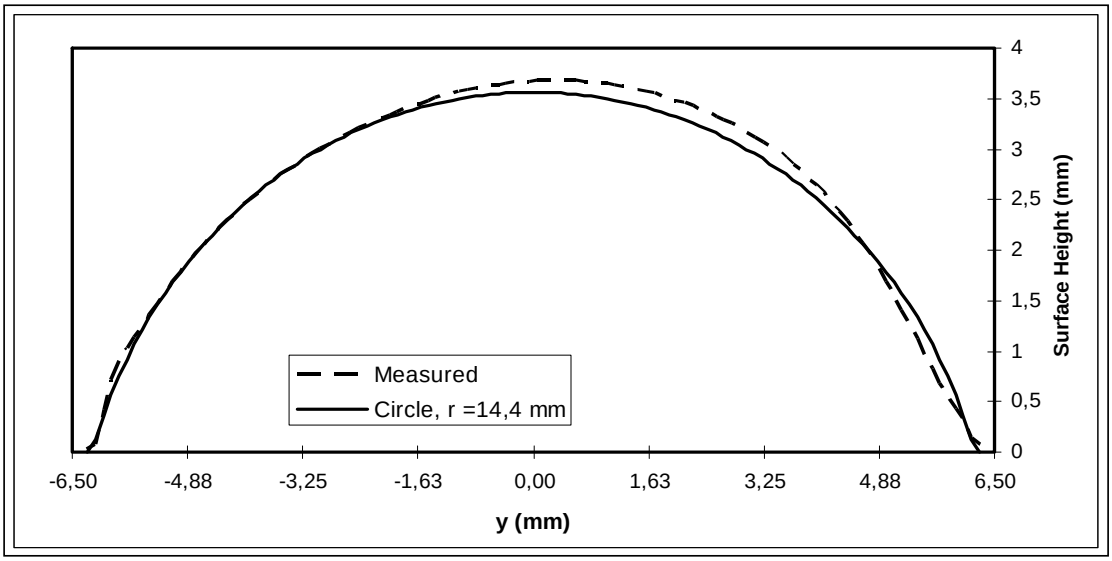

Figure 4.5. Comparison between a cross-section of the reconstructed surface with a circle of a radius 14.4 mm. The rms error is 0.4 mm.

4.3.3 Reconstruction of a triangular shaped paper

Another test object is a piece of paper which is folded into a triangular shape, as shown in Figure 4.6(a). The deformed fringe pattern is shown in Figure 4.6(b). Figure 4.6(c) shows the reconstructed surface of this object.

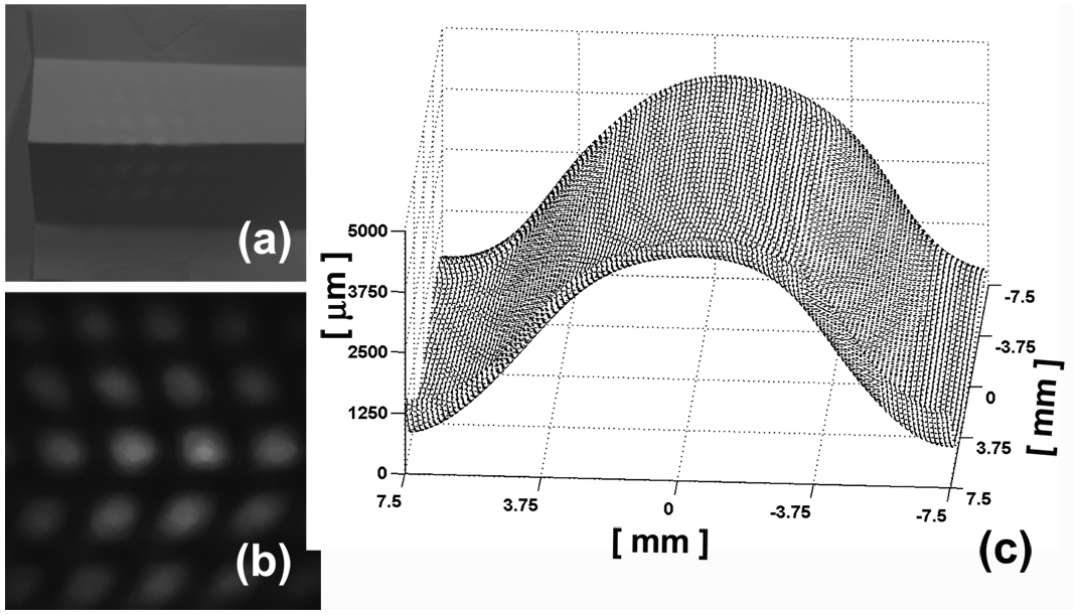

Figure 4.6. (a) Triangular shape object; (b) projected fringe pattern; (c) reconstructed surface of the object.

4.3.4 Reconstruction of a piece of sand-stone

As it is known that the speckle noise is surface dependent, and it increases significantly if one works with coarse objects due to usage of a coherent HeNe laser source. In other words, optically rough surfaces limit the resolution of the systems in optical profilometry techniques. In this experiment, the objects were profiled by a 2-D Fourier transformation and a 2-D Hanning filtering to reinforce the frequencies around the carrier frequency u_0 -as expressed in Equation 3.20- and attenuate the rest more as the distance

from u_0 is increased. The frequencies caused by speckle-like structure and the discontinuities can be minimised with this procedure [8, 31]. A piece of sand-stone that has an optically rough surface was purposely chosen to see if the method which is described above works for speckle-like objects or not. The piece of sand-stone and its analyzed surface can be seen in Figure 4.7(a). The deformed fringe pattern is shown in Figure 4.7(b). As it can be seen in Figure 4.7(c), the surface of this object was successfully profiled in spite of the speckle noise presented in the system.

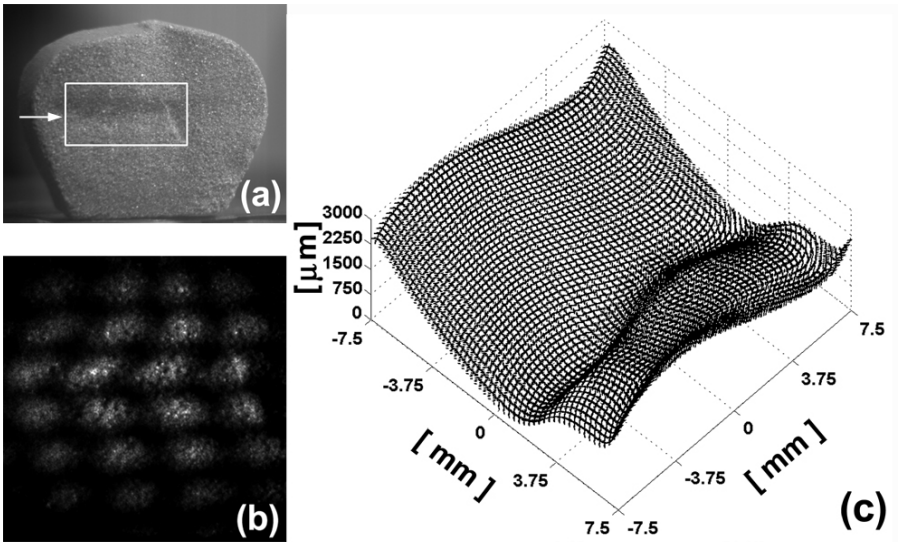

Figure 4.7. (a) A piece of sand-stone and the outlined area shows the analysed surface; (b) projected fringe pattern; (c) reconstructed surface of the object.

4.3.5 Reconstruction of a sculptured head object

Another example is a small sculptured head object; its inspected area can be seen in Figure 4.8(a). The corresponding deformed fringe pattern and the reconstructed surface is seen in Figure 4.8(b) and Figure 4.8(c), respectively.

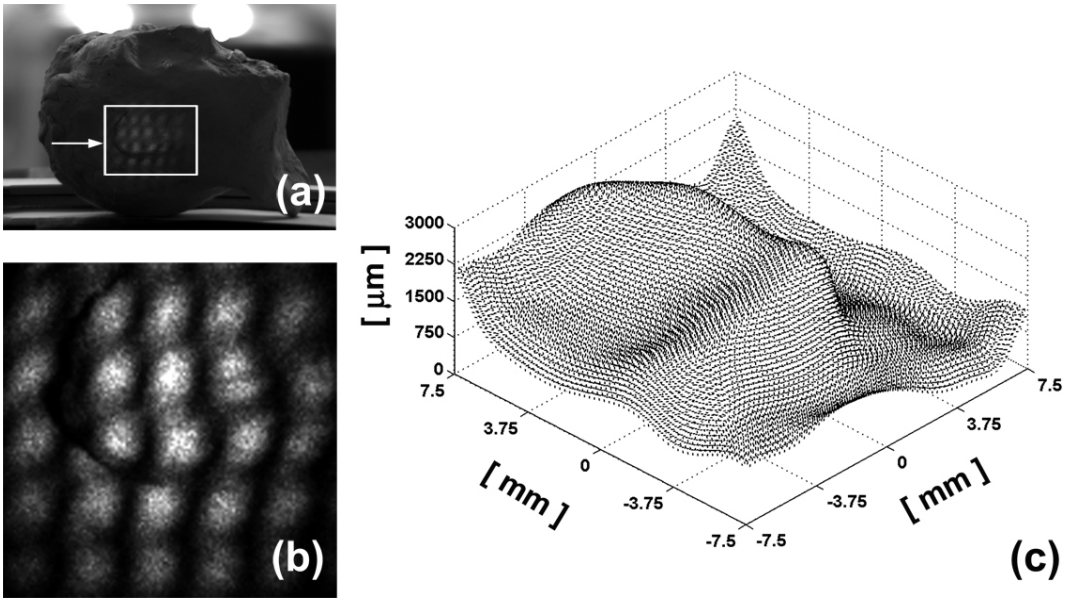

Figure 4.8. (a) Sculptured head object and the outlined area shows the analysed surface; (b) projected fringe pattern; (c) reconstructed surface of the object.

In relation to the selected object, it must be noted that this FTP technique was employed for various stone monuments of Roman Age in The National Museum of L'Aquila, Italy to assess the deteriorating action on these cultural objects [46].

As a final note, the results presented here show that such a method can be applied to relatively flat objects but we should be aware that a more sophisticated phase unwrapping algorithm might be necessary if the test object has discontinuities, for example, holes, shaded regions and cracks which may result in an abrupt phase change (larger than π) in the measurement.

4.4 Discussion

As explained above, the interference pattern was simply generated by coupling a HeNe laser beam into the cores of a four-core optical fiber located within a single cladding. The size and the cost of the system were reduced without having needed an optical fiber coupler, which is a requirement for producing multiple coherent sources in fiber optic interferometric systems to produce interference patterns. In this experimental setup, there was no requirement for an alignment or rotation of fiber ends with respect to each other to control polarization, which is a problematic procedure in other fiber optic based interferometric profilometry systems. The use of four cores and the consequent miniaturisation and compactness provided a highly visible fringe pattern, which is an important factor in terms of resolution of the system. The fixed core separation also resulted in a stable fringe pattern which makes it a candidate for *in-situ* interferometric applications in harsh environments.

The four-core fiber that has been used in this experiment has core separations of 40.6 μm, which resulted in a small number of fringes that we have effectively used (5x5 fringe pattern) and a large fringe spacing (i.e., 4.01 mm). Then, the inspectable area was limited due to this small fringe number. The large spacing of the fringes certainly decreased the sensitivity of the system. This problem can be resolved easily by choosing a larger separation of the cores, or alternatively, using smaller wavelengths for forming the fringe patterns. The four-core fiber was originally designed at the fiber telecommunication wavelengths, 1.3 μm and 1.55 μm. Therefore, each guiding fiber's (i.e., core's) cut-off wavelength was above the operating wavelength of 632.8 nm, that is, due to a large core diameter, which resulted in higher order guided modes. Bending the fiber at several points along its length terminated these modes. Such bending also decreased the number of fringes from a 9x9 pattern to a 6x6 one. It would have been more useful to design this four-core fiber with smaller core diameters and large core separations to overcome all these problems mentioned above. For example, in order to obtain more precise results for similar applications, it might be designed a four-core or a two-core fiber in a 125 μm single cladding with a mode field diameter of 4 μm (for an operating wavelength of 630 nm) and a centre-to-centre core separation of 105 μm. As it was given in Equation 3.38, the number

of fringes is directly proportional to the fiber core separations, numerical aperture and the illumination wavelength λ. It would be possible to obtain approximately 30 analysable fringes for the two-core fiber and 30x30 fringe pattern for the four-core fiber, with a 2.1 mm fringe spacing for an object distance of 0.35 m. Since the numerical aperture and the illumination wavelength were fixed for fiber cores in the interferometric system in concern, the only variable parameter that affects the fringe number is the core separation. Such a large separation of the cores would certainly increase the sensitivity of the multicore fiber interferometric system approximately by five times.

5 CONCLUSION

This research demonstrated for the first time the use of a four-core optical fiber for measurements of three-dimensional object shapes using the Fourier transform profilometry method. The structured light pattern was produced by the interference of four wave fronts emitted from each core of a four-core optical fiber. The generated interference pattern was projected on the object surface by an optimum illumination angle considering the shadowing effects. The optical setup was arranged in such geometry that only the two vertical interferograms of the six superimposed ones contained the object's height information. The deformed fringe pattern containing the object's height information was 2-D Fourier transformed. In the frequency domain, the side-lobe related the vertical interferogram was isolated via a 2D Hanning window and translated towards origin. After inverse Fourier transformation, the phase data was obtained. Then, this discontinuous phase data was converted to a continuous one by a phase-unwrapping algorithm. The shape of the object was determined by using the geometrical parameters of the setup. Various types of test objects were reconstructed by the given procedure above. The system had a depth of resolution of about 0.15 mm and the root-mean-squared error of 0.4 mm. With the aid of given theoretical analysis and acquired experiences so far, it was shown that this error can be compensated easily by redesigning the four-core fiber by choosing a larger distance of centre-to-centre core separations.

The main advantage of the proposed system can be considered as ruling out the necessity for using a fiber coupler, in an optical profilometry system, for multiple sources generation. Moreover, alignment and fixation procedure of sources are also eliminated by this system which in turn resulted in the high fringe visibility. The results show that the proposed interferometric scheme significantly reduces the system's cost and its bulkiness, and also increases its stability. Hence, it is promising for 3D measurements and its sensitivity can be further developed by manufacturing suitable multicore optical fibers.

5.1 Suggestions for Future Work

In the light of given theoretical analysis, a four-core optical fiber can be redesigned to give a satisfactory performance for an optical profilometry system. Then, a sophisticated phase unwrapping algorithm might be developed which can benefit from all six superimposed interferograms projected on the object.

This type of multicore fiber can also be used in the applications of the fields of interference lithography and laser ablation. It is possible to obtain various symmetries and shapes by designing the cores in a specific geometry. Therefore, in a single exposure step, various two-dimensional periodic patterns can be created by using a multicore fiber.

Moreover, the ability to introduce phase shifts through a little bending [12] may allow the multicore fibers to be potential candidates for structural health monitoring applications.

REFERENCES

[1] Schawlow AL, Townes HT. Infrared and Optical Masers. Phys Rev 1958; 112(6):1940-9.

[2] Meadows DM, Johnson WO, Allen JB. Generation of surface contours by Moiré patterns. Appl Opt 1970; 9(4):942-7.

[3] Dai YZ, Chiang FP. Contouring by moiré interferometry. Exp Mech 1991; 31:76-81.

[4] Srinivasan V, Liu HC, Halioua M. Automated phase-measuring profilometry of 3-D diffuse objects. Appl Opt 1984; 23:3105-8.

[5] Toyooka S, Iwasa Y. Automatic profilometry of 3-D diffuse objects by spatial phase detection. Appl Opt 1986; 25(10):3012-8.

[6] Takeda M, Mutoh K. Fourier transform profilometry for the automatic measurement of 3-D object shapes. Appl Opt 1983; 22:3977-82.

[7] Takeda M, Ina H, Kobayashi S. Fourier-transform method of fringe-pattern analysis for computer-based topography and interferometry. J Opt Soc Am 1982; 72:156-60.

[8] Bone DJ, Bachor HA, Sanderman J. Fringe-pattern analysis using a 2-D Fourier transform. Appl Opt 1986; 25(10):1653-60.

[9] Spagnolo GS, Guattari G, Sapia C, Ambrosini D, Paoletti D, Accardo G. Three-dimensional optical profilometry for artwork inspection. J Opt A-Pure Appl Opt 2000; 2:353-61.

[10] Pennington TL, Xiao H, May R, Wang A. Miniaturized 3-D surface profilometer using a fiber optic coupler. Opt Laser Technol 2001; 33:313-20.

[11] Quan C, Tay CJ, Shang HM, Bryanston-Cross PJ. Contour measurement by fibre optic fringe projection and Fourier transform analysis. Opt Comm 1995; 119:479-83.

[12] Gander MJ, Macrae D, Galliot EAC, McBride R, Jones JDC, Blanchard PM, Burnett JG, Greenaway AH, Inci MN. Two-axis bend measurement using multicore optical fibre. Opt Comm 2000; 182:115-21.

[13] Khotiaintsev KS, Svirid V, Glebova L. Laser Doppler velocimeter miniature differential probe for biomedical applications. Proc SPIE 1996; 2928(15):158-64.

[14] Stout KJ, Blunt L. Three Dimensional Surface Topography. London, Eng.: Kogan Page, second edition, 2000.

[15] Rowe SH, Welford WT. Surface topography of non–optical surfaces by projected interference fringes. Nature 1967; 216:786-7.

[16] Ghiglia DC, Mastin GA, Romero LA. Cellular–automata method for phase unwrapping. J Opt Soc Am A 1987; 4(1):267-80.

[17] Jain R, Kasturi R, Schunck B. Machine Vision. New York, USA: McGraw–Hill Inc., 1995.

[18] Hariharan P. Optical Interferometry. Australia: Academic Press, 1985.

[19] Young RD. Surface microtopography. Phys Today 1971; 24(11):42-9.

[20] Perry DM, Moran PJ, Robinson GM. Three-dimensional surface metrology of magnetic recording materials through direct-phase detecting microscopic interferometry. J Inst Electron Radio Eng 1985; 55(4):145-50.

[21] Wyant JC, Koliopoulos CL, Bhushan B, Basila D. Development of a three-dimensional noncontact digital optical profiler. J Tribol-T Asme 1986; 108(1):1-8.

[22] Lange SR, Bhushan B. Use of two- and three-dimensional noncontact surface profiler for tribology applications. Surface Topogr 1988; 1(3):277-89.

[23] Bruning JH, Herriott DR, Gallagher JE, Rosenfold DP, White AD, Brangaccio DJ. Digital wavefront measuring interferometer for testing optical surface and lenses. Appl Opt 1974; 13(11):2693-703.

[24] Peterson RW, Robinson GM, Carlsen RA, Englund CD, Moran PJ, Wirth WM. Interferometric measurement of the surface profile of moving samples. Appl Opt 1984; 23(10):1464-66.

[25] Sommargren GE. Optical heterodyne profilometry. Appl Opt 1981; 20:610-8.

[26] Pantzer D, Politch J, Ek L. Heterodyne profiling instrument for the ångström region. Appl Opt 1986; 25:4168-72.

[27] Downs MJ, McGivern WH, Ferguson HJ. Optical system for measuring the profiles of super-smooth surfaces. Prec Eng 1985; 7(4):211-5.

[28] Lessor DL, Hartman JS, Gordon RL. Quantitative surface topography determination by Nomarski reflection microscopy. 1:Theory. J Opt Soc Am 1979;69(2):357-66.

[29] Bristow TC. Surface roughness measurements over long scan lengths. Surface Topogr 1988;1(1):85-9.

[30] Makosch G, Drollinger B. Surface profile measurement with a scanning differential a/c interferometer. Appl Opt 1984; 23(24):4544-53.

[31] Lin J-F, Su X-Y. Two-dimensional Fourier transform profilometry for the automatic measurement of three-dimensional object shapes. Opt Eng 1995; 34(11):3297-302.

[32] Asundi A, Sajan MR, Tong L. Dynamic photoelasticity using TDI imaging. Opt Lasers Eng 2002; 38(1-2):3-16.

[33] Itoh K. Analysis of the phase unwrapping algorithm. Appl Opt 1982; 21(14):2470.

[34] Vrooman HA, Mass AA. Proc. FASIG 'Fringe Analysis 89', Loughborough, 1989.

[35] Robinson DW, Williams DC. Digital phase stepping speckle interferometry. Opt Comm 1986; 57:26-30.

[36] Huntley JM. Noise immune phase unwrapping algorithm. Appl Opt Lett 1989; 28:3268-70.

[37] Kwon OY, Shough DM, Williams RA. Stroboscopic phase-shifting interferometry. Opt Lett 1987; 12:855-7.

[38] Towers DP, Judge TR, Bryanston-Cross PJ. Automatic Interferogram Analysis applied to Quasi-heterodyne Holography and ESPI. Opt Lasers Eng 1991; 14:239-82.

[39] Ghiglia DC, Mastin GA, Romero LA. Cellular–automata method for phase unwrapping. J Opt Soc Am A 1987; 4(1):267-80.

[40] Green RJ, Walker JG, Robinson DW. Investigation of the Fourier-transform method of fringe pattern analysis. Opt Lasers Eng 1988; 8(1):29-44.

[41] Gåsvik KJ. Optical Metrology. West Sussex, Eng.: J. Wiley & Sons, third edition, 2002.

[42] HesFibel, http://www.hesfibel.com.tr

[43] Hecht E. Optics. Reading, Mass: Addison-Wesley, third edition, 1998.

[44] Gonzalez RC, Woods RE. Digital Image Processing. Reading, Mass.: Addison-Wesley, 1992.

[45] Berryman F, Pynsent P, Cubillo J. The effect of windowing in Fourier transform profilometry applied to noisy images. Opt Lasers Eng 2004; 41(6):815-825.

[46] Spagnolo GC, Ambrosini D, Paoletti D, Accardo G. Fibre optic projected fringes for monitoring marble surface status. J Cult Heritage 2000; 1(1):337-43.

REFERENCES

[1] Schawlow AL, Townes HT. Infrared and Optical Masers. Phys Rev 1958; 112(6):1940-9.

[2] Meadows DM, Johnson WO, Allen JB. Generation of surface contours by Moiré patterns. Appl Opt 1970; 9(4):942-7.

[3] Dai YZ, Chiang FP. Contouring by moiré interferometry. Exp Mech 1991; 31:76-81.

[4] Srinivasan V, Liu HC, Halioua M. Automated phase-measuring profilometry of 3-D diffuse objects. Appl Opt 1984; 23:3105-8.

[5] Toyooka S, Iwasa Y. Automatic profilometry of 3-D diffuse objects by spatial phase detection. Appl Opt 1986; 25(10):3012-8.

[6] Takeda M, Mutoh K. Fourier transform profilometry for the automatic measurement of 3-D object shapes. Appl Opt 1983; 22:3977-82.

[7] Takeda M, Ina H, Kobayashi S. Fourier-transform method of fringe-pattern analysis for computer-based topography and interferometry. J Opt Soc Am 1982; 72:156-60.

[8] Bone DJ, Bachor HA, Sanderman J. Fringe-pattern analysis using a 2-D Fourier transform. Appl Opt 1986; 25(10):1653-60.

[9] Spagnolo GS, Guattari G, Sapia C, Ambrosini D, Paoletti D, Accardo G. Three-dimensional optical profilometry for artwork inspection. J Opt A-Pure Appl Opt 2000; 2:353-61.

[10] Pennington TL, Xiao H, May R, Wang A. Miniaturized 3-D surface profilometer using a fiber optic coupler. Opt Laser Technol 2001; 33:313-20.

[11] Quan C, Tay CJ, Shang HM, Bryanston-Cross PJ. Contour measurement by fibre optic fringe projection and Fourier transform analysis. Opt Comm 1995; 119:479-83.

[12] Gander MJ, Macrae D, Galliot EAC, McBride R, Jones JDC, Blanchard PM, Burnett JG, Greenaway AH, Inci MN. Two-axis bend measurement using multicore optical fibre. Opt Comm 2000; 182:115-21.

[13] Khotiaintsev KS, Svirid V, Glebova L. Laser Doppler velocimeter miniature differential probe for biomedical applications. Proc SPIE 1996; 2928(15):158-64.

[14] Stout KJ, Blunt L. Three Dimensional Surface Topography. London, Eng.: Kogan Page, second edition, 2000.

[15] Rowe SH, Welford WT. Surface topography of non–optical surfaces by projected interference fringes. Nature 1967; 216:786-7.

[16] Ghiglia DC, Mastin GA, Romero LA. Cellular–automata method for phase unwrapping. J Opt Soc Am A 1987; 4(1):267-80.

[17] Jain R, Kasturi R, Schunck B. Machine Vision. New York, USA: McGraw–Hill Inc., 1995.

[18] Hariharan P. Optical Interferometry. Australia: Academic Press, 1985.

[19] Young RD. Surface microtopography. Phys Today 1971; 24(11):42-9.

[20] Perry DM, Moran PJ, Robinson GM. Three-dimensional surface metrology of magnetic recording materials through direct-phase detecting microscopic interferometry. J Inst Electron Radio Eng 1985; 55(4):145-50.

[21] Wyant JC, Koliopoulos CL, Bhushan B, Basila D. Development of a three-dimensional noncontact digital optical profiler. J Tribol-T Asme 1986; 108(1):1-8.

[22] Lange SR, Bhushan B. Use of two- and three-dimensional noncontact surface profiler for tribology applications. Surface Topogr 1988; 1(3):277-89.

[23] Bruning JH, Herriott DR, Gallagher JE, Rosenfold DP, White AD, Brangaccio DJ. Digital wavefront measuring interferometer for testing optical surface and lenses. Appl Opt 1974; 13(11):2693-703.

[24] Peterson RW, Robinson GM, Carlsen RA, Englund CD, Moran PJ, Wirth WM. Interferometric measurement of the surface profile of moving samples. Appl Opt 1984; 23(10):1464-66.

[25] Sommargren GE. Optical heterodyne profilometry. Appl Opt 1981; 20:610-8.

[26] Pantzer D, Politch J, Ek L. Heterodyne profiling instrument for the ångström region. Appl Opt 1986; 25:4168-72.

[27] Downs MJ, McGivern WH, Ferguson HJ. Optical system for measuring the profiles of super-smooth surfaces. Prec Eng 1985; 7(4):211-5.

[28] Lessor DL, Hartman JS, Gordon RL. Quantitative surface topography determination by Nomarski reflection microscopy. 1:Theory. J Opt Soc Am 1979;69(2):357-66.

[29] Bristow TC. Surface roughness measurements over long scan lengths. Surface Topogr 1988;1(1):85-9.

[30] Makosch G, Drollinger B. Surface profile measurement with a scanning differential a/c interferometer. Appl Opt 1984; 23(24):4544-53.

[31] Lin J-F, Su X-Y. Two-dimensional Fourier transform profilometry for the automatic measurement of three-dimensional object shapes. Opt Eng 1995; 34(11):3297-302.

[32] Asundi A, Sajan MR, Tong L. Dynamic photoelasticity using TDI imaging. Opt Lasers Eng 2002; 38(1-2):3-16.

[33] Itoh K. Analysis of the phase unwrapping algorithm. Appl Opt 1982; 21(14):2470.

[34] Vrooman HA, Mass AA. Proc. FASIG 'Fringe Analysis 89', Loughborough, 1989.

[35] Robinson DW, Williams DC. Digital phase stepping speckle interferometry. Opt Comm 1986; 57:26-30.

[36] Huntley JM. Noise immune phase unwrapping algorithm. Appl Opt Lett 1989; 28:3268-70.

[37] Kwon OY, Shough DM, Williams RA. Stroboscopic phase-shifting interferometry. Opt Lett 1987; 12:855-7.

[38] Towers DP, Judge TR, Bryanston-Cross PJ. Automatic Interferogram Analysis applied to Quasi-heterodyne Holography and ESPI. Opt Lasers Eng 1991; 14:239-82.

[39] Ghiglia DC, Mastin GA, Romero LA. Cellular–automata method for phase unwrapping. J Opt Soc Am A 1987; 4(1):267-80.

[40] Green RJ, Walker JG, Robinson DW. Investigation of the Fourier-transform method of fringe pattern analysis. Opt Lasers Eng 1988; 8(1):29-44.

[41] Gåsvik KJ. Optical Metrology. West Sussex, Eng.: J. Wiley & Sons, third edition, 2002.

[42] HesFibel, http://www.hesfibel.com.tr

[43] Hecht E. Optics. Reading, Mass: Addison-Wesley, third edition, 1998.

[44] Gonzalez RC, Woods RE. Digital Image Processing. Reading, Mass.: Addison-Wesley, 1992.

[45] Berryman F, Pynsent P, Cubillo J. The effect of windowing in Fourier transform profilometry applied to noisy images. Opt Lasers Eng 2004; 41(6):815-825.

[46] Spagnolo GC, Ambrosini D, Paoletti D, Accardo G. Fibre optic projected fringes for monitoring marble surface status. J Cult Heritage 2000; 1(1):337-43.